

Article

Analysis of Structural, Optical, and Magnetic Properties of (Fe,Co) Co-Doped ZnO Nanoparticles Synthesized under UV Light

Nawal Madkhali 

Physics Department, College of Sciences, Imam Mohammad Ibn Saud Islamic University (IMSIU),
Riyadh 13318, Saudi Arabia; namadkhali@imamu.edu.sa

Abstract: In this report, we discuss the preparation of undoped and (Fe,Co) co-doped ZnO nanocomposites via an ultrasonicated probe, which were both under UV irradiation for 12 h and annealed at 400 °C for four hours in ambient air. Here, we investigated the different concentration of dopant transition metals (ZnO-Fe_{1-x}-Co_x) (x = 0.03, 0.05, and 0.07). X-ray diffraction (XRD) analyses confirmed the nanophase, crystallinity, good uniformity, and around 28 nm core sizes of all of the (ZnO-Fe_{1-x}-Co_x) as-synthesized composites with different rates. The optical properties of ZnO doped with a high percent of Fe nanoparticles displayed an increase in absorption in the UV region and a slight decrease in the energy band gap to 3.13 eV. Magnetic measurements revealed that doping enhanced the ferromagnetism of ZnO. Recent studies which aimed to improve the optical and magnetic properties of metal oxides, the most important of which being zinc oxide, have allowed their applications to diversify and multiply in the medical, industrial, and electronic fields.

Keywords: nanocomposites; ZnO nanoparticles; ferromagnetism; band gap; VSM



Citation: Madkhali, N. Analysis of Structural, Optical, and Magnetic Properties of (Fe,Co) Co-Doped ZnO Nanoparticles Synthesized under UV Light. *Condens. Matter* **2022**, *7*, 63. <https://doi.org/10.3390/condmat7040063>

Academic Editor: Víctor Manuel García Suárez

Received: 24 August 2022
Accepted: 25 October 2022
Published: 8 November 2022

Publisher's Note: MDPI stays neutral with regard to jurisdictional claims in published maps and institutional affiliations.



Copyright: © 2022 by the author. Licensee MDPI, Basel, Switzerland. This article is an open access article distributed under the terms and conditions of the Creative Commons Attribution (CC BY) license (<https://creativecommons.org/licenses/by/4.0/>).

1. Introduction

One of the global scientific community's most important research focuses concerns the development of advanced nanocomposite materials for applications in the photocatalysis, optoelectronic, and semiconducting industries. ZnO has a stable hexagonal wurtzite (WZ) structure, a wide band gap semiconductor with a band gap from 3.10 to 3.37 eV at room temperature, and a large exciton binding energy of 60 meV. These structural advantages mean that zinc oxide could be applied in various fields, such as in gas sensors; in this field, its application depends on its ability to change electrical conductivity to enable a change in gas concentration [1] (ZnO has also been widely used in solar cells and hybrid solar cells with organic compounds due to its outstanding properties such as low cost, high stability, and environmentally friendly materials [2] In medical applications, zinc oxide is used in sunscreen creams due to its stability and inherent capability to absorb UV irradiation [3]. All of these features mean that for many years, zinc oxide has been of interest to researchers.

In addition, different preparation methods through the addition of transition metals can be used to improve these properties and expand the promising fields of application for zinc oxide compounds. In the past few years, scientists have investigated the effect of doping ZnO nanoparticles (NPs) with 3D transition metals such as Fe and Co. In many studies, it has been suggested that transition metal doping in ZnO NPs leads to a change in their magnetic properties. This means they have potential applications in spintronics devices, such as spin field-effect transistors [4], gas sensors [5] and quantum dot light-emitting diodes [6]. This means that (Fe,Co) co-doped ZnO is one of the most promising candidates for use as dilute magnetic oxide (DMO) oxide materials. Nevertheless, doping with various transition metals is one of the excellent techniques to modify the diverse dielectric properties such as dielectric constant and loss energy, which highlights its importance in electric storage applications. Newly, saddi et al [7] show how the increase in Fe ion concentration doped with ZnO enhanced the dielectric properties in the 40–10⁷ Hz frequency range.

Recently, in the field of spintronics applications, diluted magnetic oxides (DMOs) have been a major focus of numerous studies [8]. The recent progress in improving the magnetic nature that can make metal oxides such as zinc oxide doped with ferro materials have applications in new fields that were not within its applied fields such as hyperthermia and magnetic resonance imaging (MRI) [9].

Nowadays, an increasing number of researchers have shown interest in the modification of the magnetic and optical properties of semiconductors by creating crystal defects. These defects are caused by transition metal ions that improve the properties of metal oxides such as zinc oxide and titanium dioxide [10]. Beltrán et al. [11] reported on the very good heating ability of ferrimagnetic disordered spinel, and when the annealing time was increased from 1 h to 3 h, there was the possibility of oxygen vacancies and zinc vacancies. Using the XAFS technique, the oxidation state of cation atoms could be obtained. Fe and Co preferentially substitute Zn in a ZnO structure in 2+ and 3+ oxidation states for Co and Fe ions, respectively [12]. Recent advances in different technologies have prompted researchers to generate different synthesis methods based on changing the structure of materials, for example, using metal-organic frameworks (MOFs) has realized the transformation from six-pointed stars, flower-like, and cube-like to random stone-like, thanks to its special morphology and balanced magnetic dielectric multi-loss mechanism [13].

Many scientific papers have been published regarding different preparation methods, such as the solvothermal method [14] microwave heating technology [15], and pulsed-laser deposition [16]. The effect of cobalt on the magnetic properties of zinc oxide has also been studied. However, this topic is still being researched due to the interference of foreign phases not caused by the presence of Co⁺⁺ ions [17]. In Table 1, different methods used to obtain ZnO(TM) nanostructures are shown.

Table 1. Examples of ZnO(TM) nanostructures obtained using various methods.

No.	Type of Nanostructure	Method	References
1	Fe-doped ZnO	Spin coating	[18]
2	Fe-doped ZnO	Chemical spray pyrolysis	[19]
3	(Al, Fe) co-doped ZnO	Sol-gel method	[20]
4	(Al, Fe) co-doped ZnO	Co-precipitation process	[21]
5	Co-doped ZnO	Pulsed-laser deposition (PLD)	[16]
6	Fe- and Co-doped ZnO	Mechanical milling	[12]
7	Co-doped ZnO	Sol-gel method	[22]
8	Co-doped ZnO	Hydrothermal method	[23]
9	Fe- and Co-doped ZnO	Sol-gel method	[24]
10	Fe- and Co-doped ZnO	Ultrasonication probe under UV radiation	This work

The improvement of the optical properties of zinc oxide is no less important than the enhancement of the magnetic properties of zinc oxide by adding transition metals. Photoluminescence spectroscopy measurements indicated more reductions in the green, orange, and red visible emission regions after the addition of Ni and Co ions compared to pure ZnO [25]. Various papers indicated the influence of Co ions in the formation of multi-emission centers below the band gap energy of ZnO [23]. Many transition metals (TMs) are used as dopants in ZnO to improve the photocatalytic activity of the ZnO spectrum. For instance, Ag acts as a p-dopant in the ZnO crystal lattice. The optical efficiency of zinc oxide was doubled in the presence of silver by 0.32%wt [26]. However, the structural defects introduced by Fe²⁺ ions, such as a large surface and roughness, were shown to enhance the absorption of thin films, and consequently, the optical transmittance decreased [27].

Recently, various studies revealed that the presence of irradiation increases the crystalline defects of nanomaterials, which can improve the physical properties of a material. For example, the photoinduced high polarizabilities of excited states were shown to provide applications in refraction. In addition, the nonlinear optical (NLO) and the optical elastic scattering properties of native defect-rich ZnO [28].

The ease of the irradiation techniques used in the synthesis of materials and obtaining good results in improving the optical and magnetic properties of zinc oxide with transition metals opens prospects for benefiting from irradiation using ultraviolet rays in nanotechnology in terms of availability and ease of handling. In this work, we used the ultrasonication technique under UV radiation for synthesis because it is cost-effective and improves the properties of the resulting materials by increasing the crystal defects. The influence of Fe and Co doping on the structural, optical, and magnetic properties of ZnO NPs was investigated using X-ray diffraction (XRD), UV-Vis, and a vibrating sample magnetometer (VSM). In this structural study, it was observed that the incorporation of Co and Fe on ZnO NPs changes the optical properties and lattice constant values.

2. Sample Preparation

All of the chemical reagents used in the experiment were purchased from Sigma Aldrich. Zinc oxide nanopowder (50 nm particle size), iron(III) oxide hydrate ($\text{Fe}_2\text{H}_2\text{O}_4$), and cobalt(II) chloride hexahydrate ($\text{CoCl}_2 \cdot 6\text{H}_2\text{O}$) were used. Nanopowder samples of nominal compositions of $\text{ZnO-Fe}_{1-x}\text{-Co}_x$ ($x = 0.03, 0.05, \text{ and } 0.07$, hereafter referred to as $(\text{Fe}_{30}\text{Co}_{70})\text{ZnO}$, $(\text{Fe}_{50}\text{Co}_{50})\text{ZnO}$, and $(\text{Fe}_{70}\text{Co}_{30})\text{ZnO}$, respectively) were synthesized via a standard solid-state reaction route. In this experiment, the ultrasonication probe technique was used (Ultrasonic Dismembrator model 500, Fisher Scientific) for around 12 h with wavelengths of 254 nm, as shown in Figure 1. The beaker was tightly clamped, and the probe was inserted directly into the center of the beaker to dissolve appropriate amounts of ZnO nanoparticle powder with various ratios of Fe and Co in 100 mL of deionized water in three solutions. The resulting solutions, which ranged from gray to dark gray, were obtained by increasing the concentrations of $\text{CoCl}_2 \cdot 6\text{H}_2\text{O}$ and $\text{Fe}_2\text{H}_2\text{O}_4$. The three resultant solutions were dried. The final powder was annealed at 400 °C for 4 h in air. After this step, the powdered samples were used directly.

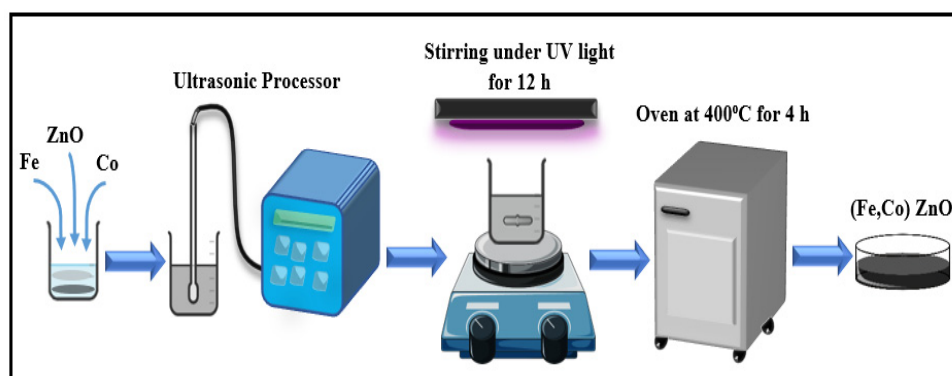


Figure 1. Schematic of the process steps followed for the synthesis of (Fe,Co) ZnO.

3. Characterization Techniques

In this experiment, the optical, structural, and magnetic properties of (Fe,Co)-doped ZnO NPs synthesized as powder samples were studied. X-ray diffraction (XRD) analysis was carried out using a Bruker D8 Discover diffractometer (θ - 2θ) equipped with $\text{Cu-K}\alpha$ radiation ($\lambda = 1.5406 \text{ \AA}$). The magnetic properties were determined using a vibrating sample magnetometer (VSM) (Quantum Design MPMS-5S SQUID magnetometer). The zero-field-cooled and field-cooled (ZFC-FC) curves were recorded at a magnetic field of 250e. Characteristic UV-Vis spectra were measured using a Shimadzu UV Probe UV-1650PC double beam, and its wavelength range was 300–800 nm, the wavelength accuracy

was ± 0.5 nm, and the photometric accuracy was ± 0.2 . The results were collected in the spectral range of 300–800 nm using rectangular quartz cuvettes.

4. Results

4.1. Structural Studies

Figure 2 illustrates the typical XRD patterns of pure ZnO and (Fe,Co) co-doped ZnO NPs synthesized via ultrasonication probe technique under UV radiation. The peak positions in this figure indicate that all the samples were nanocrystalline powder with hexagonal wurtzite structures, which is in good agreement with the standard spectrum (COD card No. 01-076-0704). The 2θ peaks appeared at 31.90° , 34.55° , 36.39° , 47.74° , 56.70° , 62.96° , and 68.11° , which were compatible with the (hkl) plane of (100), (002), (101), (102), (110), (103), and (112). The characteristic peaks of planes (100), (002), and (101) of co-doped ZnO samples shift compared to those of the undoped ZnO. This shifting shows that iron ions and cobalt ions substitute the ZnO site by their smaller ionic radii of 0.064 and 0.065 nm, respectively, compared to zinc ions (0.074 nm).

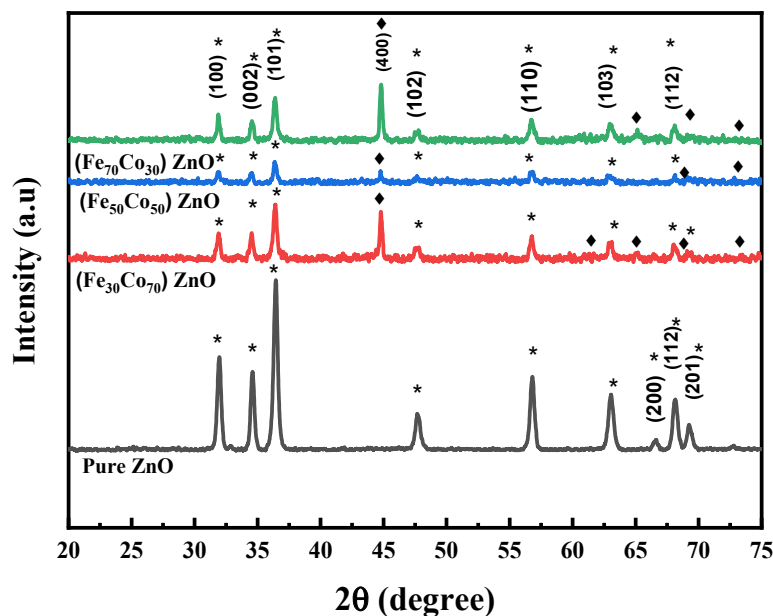


Figure 2. XRD patterns of the pure and (Fe,Co) co-doped ZnO NPs.

Otherwise, a diffraction peak at 45° appeared for all the co-doped samples, which limited the Co solubility in ZnO. this peak could coincide with the Co_3O_4 reference code (COD card No. 96-900-5898). Furthermore, no peaks of Fe or its oxides appeared in the XRD patterns, indicating that the Fe-dopant atoms were an excellent substitute for Zn atoms.

The average crystalline size was estimated using Equation (1), and the lattice parameters were calculated using Equation (2)

$$D = \frac{0.9\lambda}{\beta \cos \theta} \tag{1}$$

$$\frac{1}{d_{hkl}^2} = \frac{4}{3} \left[\frac{h^2 + hk + l^2}{a^2} \right] + \frac{l^2}{c^2} \tag{2}$$

where D is the diameter of NPs, λ is the wavelength of the X-ray (1.5406 \AA), θ is the Bragg angle, and β is the full width at half maximum (FWHM) on the intensive peak (101).

Obtained values are enlisted in Table 2. According to Table 2, one can conclude that the lattice parameter values for co-doped samples are almost similar, suggesting that the dopant Fe and Co atoms are incorporated in the ZnO lattice and substitute the Zn atom

site without changing the wurtzite structure. Nevertheless, the decrease in the intensity of diffraction at the peaks of zinc oxide with the increase in the concentration of iron and cobalt ions indicates that the crystalline character of zinc oxide has decreased, while the disappearance of some peaks clearly indicates the nature of the reduction of grain size and the presence of strain in the ZnO due to the induction of metal ions

Table 2. Particle size and lattice parameters a, c, and c/a of ZnO, (Fe₃₀Co₇₀) ZnO, (Fe₅₀Co₅₀) ZnO, and (Fe₇₀Co₃₀) ZnO NPs.

Samples	Grain Size (nm)	a = b (Å)	c (Å)	c/a
ZnO	21.4 ± 0.3	3.2299	5.1789	1.6034
(Fe ₃₀ Co ₇₀)ZnO	25.2 ± 0.8	3.2365	5.1991	1.6064
(Fe ₅₀ Co ₅₀) ZnO	24.2 ± 0.5	3.2353	5.1893	1.6039
(Fe ₇₀ Co ₃₀) ZnO	23.5 ± 0.1	3.2355	5.1842	1.6023

The structural lattice parameters of the different samples' compositions were evaluated using the relations:

$$a = \lambda / \sqrt{3} \sin \theta_{(100)} \text{ and } c = \lambda / \sin \theta_{(002)}$$

where λ is the wavelength of the CuK α radiation (1.5405 Å) and θ_{hkl} is the diffraction angle.

The average particle size is listed in Table 2 and was found to decrease with the increase in Fe-doping concentration, thereby supporting the XRD analysis which refers to the compressive strain that may be imposed on the crystal growth by Lorentz force processing. As it is affected by the small radius of Fe-doping ions, this suggests that increasing the Fe ion concentration decrease the average crystallite size for doped samples (Tariq et al., 2019). The lattice parameters (a and c) do not show any significant change compared to those of the undoped ZnO except for a slight change for the (Fe₃₀Co₇₀) ZnO sample. This could be attributed to the substitution of the ZnO with Co or/and Co₂O₃ ions in the hexagonal structure.

4.2. Optical Properties

4.2.1. Absorption

The optical properties of pure ZnO and (Fe,Co)-doped ZnO nanopowder synthesized using a spinning rod under UV light were studied via UV-Vis absorption spectroscopy. The optical absorption spectra of the pure ZnO and of the different levels of (Fe,Co)-doped ZnO NPs were investigated in the wavelength range of 300–800 nm.

Figure 3 shows the absorption spectra of the pure ZnO, (Fe₃₀Co₇₀)ZnO, (Fe₅₀Co₅₀)ZnO, and (Fe₇₀Co₃₀)ZnO NPs with absorption peaks at 362, 354, 358, and 354 nm, respectively. The interpretation of optical properties in semiconductors consisting of metal oxide nanostructures is attributed to various factors, such as the size of the particles, flaws or deformities in the grain structure, and oxygen deficiencies (Pal Singh et al., 2016a). We clearly observed that zinc oxide nanoparticles had high light absorption in the area of ultraviolet radiation and that this absorption decreased exponentially and gradually in the visible light area (approximately 400 nm) (Pal Singh et al., 2016; Park and Koh, 2013). The absorption maximum became higher than that of the other samples (pure ZnO and samples with different levels of Fe,CO) when the Fe-doping level was 70% and the Co-doping level was 30%. Additionally, we noticed that the absorption in the visible light area (from 400 nm to 700 nm) increased due to the smaller size of the nanoparticles, as evident from the XRD results, and the well-known d-d transitions (Pal Singh et al., 2016) were clearly displayed at approximately 410 nm and 667 nm when the Fe-doping levels increased to 50% and 70%. Furthermore, an obvious blueshift of the absorption edges could be observed in the (Co,Fe)-doped ZnO samples from 362 to 353 nm. It is worth mentioning that the wide and long absorption range in the visible region from wavelength 450 nm to about 650 nm, which clearly appeared as a result of the increase in iron concentration, was evidence of the presence of oxygen vacancies (or iron centers), resulting in crystal defects which improved

the optical absorption properties of zinc oxide, and this is consistent with the results of [29]. The peak around 670 nm decreases with the increase of Co percentage due to sp-d exchange interactions between delocalized electrons of the host lattice and localized d-electrons of cobalt ions substituting for zinc ions [30].

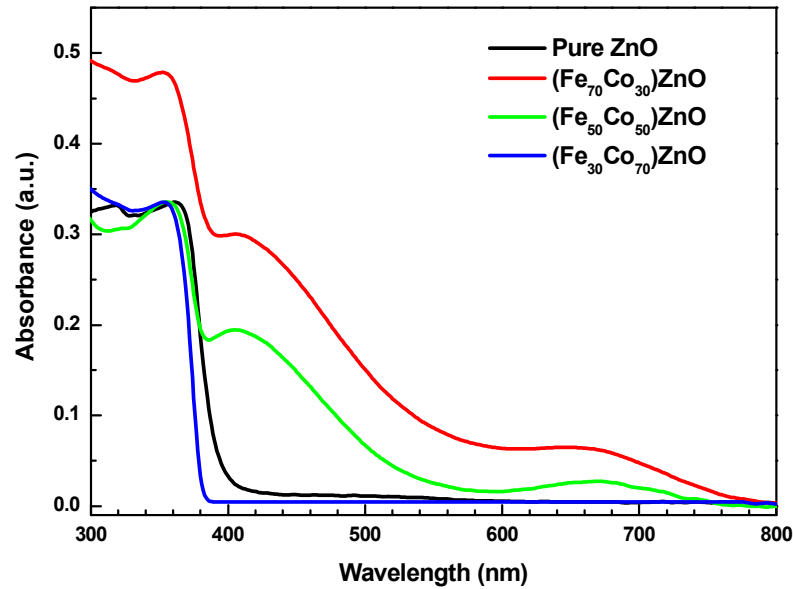


Figure 3. The UV-Vis absorbance spectrum of pure ZnO, (Fe₃₀Co₇₀)ZnO, (Fe₅₀Co₅₀)ZnO, and (Fe₇₀Co₃₀)ZnO NPs.

4.2.2. Band Gap

The optical band gap was determined by the Tauc relation given by Tauc (1968):

$$\alpha h\nu = A (h\nu - E_g)^n \tag{3}$$

where α is the absorption coefficient, h is Planck’s constant, A is a constant, ν is the photon frequency, E_g is the energy band gap, and n is equal to $\frac{1}{2}$ for a direct band gap semiconductor. The E_g estimate could be obtained by plotting $(\alpha h\nu)^2$ versus $h\nu$ and extrapolating the linear portion of the plot to the energy axis. Figure 4 shows the plots of $(\alpha h\nu)^2$ versus $h\nu$ for the pure ZnO and doped ZnO samples.

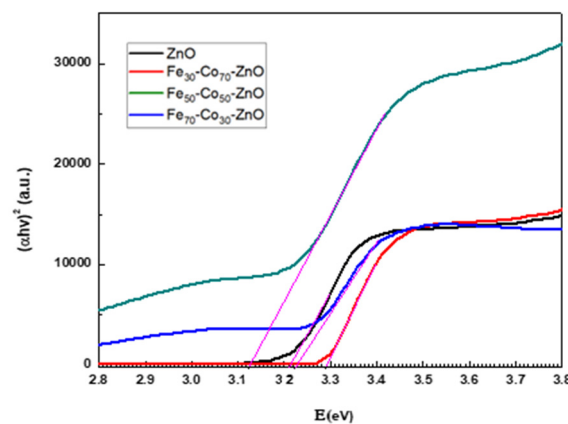


Figure 4. Tauc plots for different samples used to calculate the band gap.

From Table 3, it can be concluded that compared to that of pure ZnO, the energy band gap increased with an increasing Co-doping concentration (decrease in Fe-doping concentration) from 3.13 eV to 3.29 eV. The increase in the value of the energy band gap in

(Co,Fe)-doped ZnO NPs has been attributed to the sp-d spin exchange interaction between the localized d electron and band electrons of doped and co-doped transition metal ions substituting the vacancy of a cation [31].

Table 3. Experimental values for the band gap variations in pure ZnO, (Fe₃₀Co₇₀)ZnO, (Fe₅₀Co₅₀)ZnO, and (Fe₇₀Co₃₀)ZnO.

Urbach Energy (eV)	Band Gap (eV)	Absorption Wavelength (nm)	Sample
0.319	3.221	385.1	ZnO
0.095	3.293	376.9	Fe ₃₀ Co ₇₀ ZnO
0.1757	3.230	383.9	Fe ₅₀ Co ₅₀ ZnO
0.922	3.131	396.2	Fe ₇₀ Co ₃₀ ZnO

However, when the Fe concentration was 70% and the Co concentration was 30%, the band gap energy decreased to 3.13 eV because more charge carriers were created by the high concentration of doped Fe, which induced absorption and reduced the band gap. It is believed that a dual band gap occurs due to mixed crystalline phases or weak crystalline properties caused by Co and Fe ions.

For more about the enhanced optics, the Urbach energy has been listed in Table 3 and Figure 5. Urbach energy describes the cavity exponential broadening of absorption edge related to the thermal and disorder structural model of semiconductors, either amorphas or crystalline. According to this concept, the Urbach energy is determined by the exponential of an empirical optical gap, which is defined according to the following relation known as the Urbach relation:

$$\alpha = \alpha_0 \exp\left(\frac{hv}{E_u}\right)$$

where α is the absorption coefficient, α_0 is a characteristic parameter depending on the material, hv is the incident photon energy, and E_u is Urbach energy. The calculated values are in the interval 95 to 922 meV, while the E_u values of ZnO increase due to metal doping which emphasizes the increase in the defects density and localized energy states. This result is well-matched with the XRD and magnetic measurements.

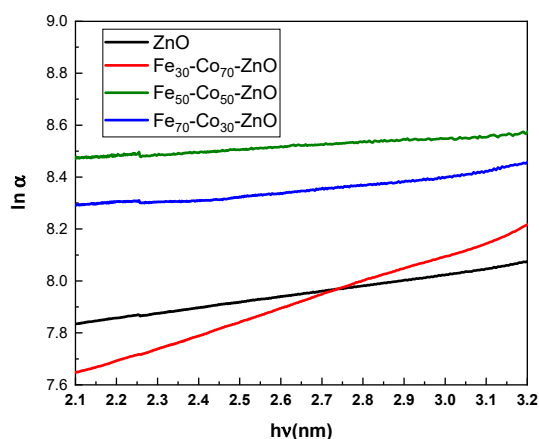


Figure 5. Urbach energy in pure ZnO and doped (Fe₃₀Co₇₀)ZnO, (Fe₅₀Co₅₀)ZnO, and (Fe₇₀Co₃₀)ZnO.

4.2.3. Magnetic Properties

To describe the magnetization properties of materials, the magnetic properties at room temperature should be recorded. The properties were recorded as hysteresis of magnetization (M) versus applied magnetic field (H) curves for pure ZnO NPs and doped ZnO: (Fe₃₀Co₇₀)-ZnO, (Fe₅₀Co₅₀)-ZnO, and (Fe₇₀Co₃₀)-ZnO NPs at different applied magnetic fields are shown in Table 4. From the hysteresis loops in Figure 6, it can be seen that

the magnetic parameters such as coercivity (H_c), saturation, and remanent magnetization (M_r) varied nonlinearly with the increases in Co and Fe ions in the ZnO lattice, as shown in Table 4. As the Fe ions' dopant ion concentration increased, the coercivity gradually increased. On the other hand, we found that the magnetism reached the highest value with the increase in cobalt ions. Additionally, it could clearly be seen that the presence of cobalt and iron ions increased the magnetism of zinc oxide regardless of the percentage of doping; this was due to the structural properties of these heavy atoms, which have paramagnetic properties because of their atomic structure in 3D orbit, and the carriers involved in carrier-mediated exchange were by-products of defects created in ZnO. Additionally, these results are in good agreement with [24].

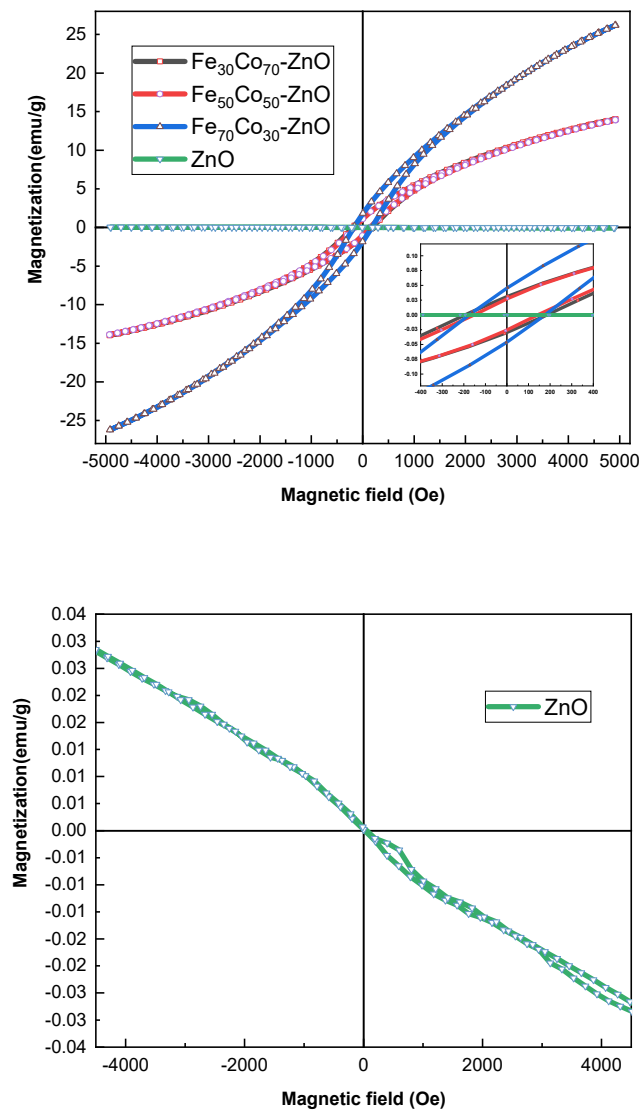


Figure 6. Hysteresis loops (M-H) from VSM measurement spectrum of pure ZnO, (Fe₃₀Co₇₀)ZnO, (Fe₅₀Co₅₀)ZnO, and (Fe₇₀Co₃₀)ZnO NPs.

Table 4. Magnetic parameters deduced from VSM measurements.

Sample	H_c (Oe)	M_r (emu/g)	M_s (emu/g)
ZnO	20.98	3.06×10^{-4}	3.43×10^{-2}
(Fe ₃₀ Co ₇₀)ZnO	137.71	1.24	14
(Fe ₅₀ Co ₅₀)ZnO	140.01	1.12	13.92
(Fe ₇₀ Co ₃₀)ZnO	151.25	1.80	26.16

Thus, we expect that ferromagnetic behavior arises from the intrinsic exchange interaction of magnetic moments in iron- and cobalt-doped ZnO. The strong ion exchange interaction mechanism of Fe and Co atoms (filled $3d^{10}$ was converted to $3d^6$ and $3d^2$ shell was converted to $3d^6$) improved the ferromagnetic behavior of ZnO after being doped. Specifically, the coupling between the delocalized p and s orbitals of 2p O and 2p Fe orbitals provided electrical channels for electron transfer in Fe and Co (Pal Singh et al., 2015). In Fe and Co co-doped ZnO, the bound magnetic polaron BMP model (Coey et al., 2005), is recommended, which causes oxygen vacancy-mediated exchange interactions between the spin-localized electrons of doped transition ions, where, oxygen vacancies play a significant role and make a sufficient contribution to the ferromagnetic in ZnO-based on diluted magnetic semiconductors systems (Pekar et al., 2021). These results are consistent with what we obtained in the optical properties as well as the structural properties from XRD. This finding is in agreement with [29,32,33].

These findings may help us to understand the changes in the foreign phases of the zinc oxide structure resulting from the formation of crystal defects in the crystal semiconductor. This in turn contributed to the improvement of the magnetic properties, which aided in finding more voids; this distinctive feature makes zinc oxide a candidate for spintronic applications. Moreover, studies in the same field indicate that the magnetic anisotropy may have possibly originated from orbital states in the TMs impurity band and the magnetization anisotropy is due to the trapping of electrons between orbital states, which could simplify an increase in the spin-orbit transitions interaction strength caused by symmetry breaking at host lattice defects [34,35].

5. Conclusions

In this study, the magnetic and optical properties of ZnO co-doped with Fe and Co ions were investigated in powder samples prepared using the UV radiation method. XRD studies indicated that the addition of 3d transition metals such as Fe and Co can cause defects in ZnO. Based on our observation that the physical and chemical properties of zinc oxide at room temperature improved significantly after adding cobalt and iron ions, we can attribute this to several reasons: defect-related causes, the formation of the second magnetic phase, and the formation of magnetic clusters of doping elements. Optical measurements revealed that the band gap changed due to the incorporation of oxygen vacancy Fe and Co ions. Moreover, Co and Fe ions with different concentrations in ZnO play a key role in the ferromagnetic mechanism, helping to achieve better performances in terms of the remaining magnetization, saturation magnetization, and coercivity. These modified properties as a result of the structural changes of zinc oxide, which was prepared in the presence of ultraviolet rays, may open wider horizons in electronic and spintronic applications for metal oxides, according to the bound magnetic polaron (BMP) model.

Funding: The authors extend their appreciation to the Deanship of Scientific Research at Imam Mohammad Ibn Saud Islamic University for funding this work through Research Group no. RG-21-09-53.

Institutional Review Board Statement: Not applicable.

Informed Consent Statement: Not applicable.

Data Availability Statement: The data presented in this study are available upon request from the corresponding author.

Acknowledgments: We acknowledge the funding received from the Deanship of Scientific Research at Imam Mohammad Ibn Saud Islamic University.

Conflicts of Interest: The author declares no conflict of interest.

References

1. Chakraborty, D.; Gayen, R.; Hussain, S.; Bhar, R.; Ghoshal, A.K.; Pal, A.K. ZnO/Ti Thin Film: Synthesis, Characterization and Methane Gas Sensing Property. *J. Phys. Conf. Ser.* **2012**, *390*, 012065. [[CrossRef](#)]
2. Yan, D.; Yin, G.; Huang, Z.; Li, L.; Liao, X.; Chen, X.; Yao, Y.; Hao, B. Cellular Compatibility of Biomineralized ZnO Nanoparticles Based on Prokaryotic and Eukaryotic Systems. *Langmuir* **2011**, *27*, 13206–13211. [[CrossRef](#)] [[PubMed](#)]
3. Liu, X.; Pan, L.; Zhao, Q.; Lv, T.; Zhu, G.; Chen, T.; Lu, T.; Sun, Z.; Sun, C. UV-assisted photocatalytic synthesis of ZnO-reduced graphene oxide composites with enhanced photocatalytic activity in reduction of Cr(VI). *Chem. Eng. J.* **2011**, *183*, 238–243. [[CrossRef](#)]
4. Guo, N.; Xiao, L.; Gong, F.; Luo, M.; Wang, F.; Jia, Y.; Chang, H.; Liu, J.; Li, Q.; Wu, Y.; et al. Light-Driven WSe₂-ZnO Junction Field-Effect Transistors for High-Performance Photodetection. *Adv. Sci.* **2019**, *7*, 1901637. [[CrossRef](#)] [[PubMed](#)]
5. Kumar, R.; Al-Dossary, O.; Kumar, G.; Umar, A. Zinc Oxide Nanostructures for NO₂ Gas-Sensor Applications: A Review. *Nano-Micro Lett.* **2014**, *7*, 97–120. [[CrossRef](#)]
6. Kim, J.-S.; Kang, B.-H.; Jeong, H.-M.; Kim, S.-W.; Xu, B.; Kang, S.-W. Quantum dot light emitting diodes using size-controlled ZnO NPs. *Curr. Appl. Phys.* **2018**, *18*, 681–685. [[CrossRef](#)]
7. Saadi, H.; Benzarti, Z.; Rhouma, F.I.H.; Sanguino, P.; Guermazi, S.; Khirouni, K.; Vieira, M.T. Enhancing the electrical and dielectric properties of ZnO nanoparticles through Fe doping for electric storage applications. *J. Mater. Sci. Mater. Electron.* **2021**, *32*, 1536–1556. [[CrossRef](#)]
8. Mishra, A.; Das, D. Investigation on Fe-doped ZnO nanostructures prepared by a chemical route. *Mater. Sci. Eng. B* **2010**, *171*, 5–10. [[CrossRef](#)]
9. da Silva, B.L.; Abuçafy, M.P.; Manaia, E.B.; Junior, J.A.O.; Chiari-Andréo, B.G.; Pietro, R.C.R.; Chiavacci, L.A. Relationship Between Structure And Antimicrobial Activity of Zinc Oxide Nanoparticles: An Overview. *Int. J. Nanomed.* **2019**, *14*, 9395–9410. [[CrossRef](#)]
10. Yadav, R.S.C. Nanostructured ZnO, ZnO-TiO₂ And ZnO-Nb₂O₅ As Solid State Humidity Sensor. *Adv. Mater. Lett.* **2012**, *3*, 197–203. [[CrossRef](#)]
11. Beltrán, J.J.; Barrero, C.A.; Punnoose, A. Understanding the role of iron in the magnetism of Fe doped ZnO nanoparticles. *Phys. Chem. Chem. Phys.* **2015**, *17*, 15284–15296. [[CrossRef](#)] [[PubMed](#)]
12. Meyer, M.; Damonte, L. Study of Co and Fe-doped ZnO milled nanopowders. *Powder Technol.* **2015**, *286*, 371–377. [[CrossRef](#)]
13. Yang, K.; Cui, Y.; Wan, L.; Zhang, Q.; Zhang, B. MOF-derived magnetic-dielectric balanced Co@ZnO@N-doped carbon composite materials for strong microwave absorption. *Carbon* **2022**, *190*, 366–375. [[CrossRef](#)]
14. Djerdj, I.; Jagličić, Z.; Arčon, D.; Niederberger, M. Co-Doped ZnO nanoparticles: Minireview. *Nanoscale* **2010**, *2*, 1096–1104. [[CrossRef](#)]
15. Wojnarowicz, J.; Chudoba, T.; Majcher, A.; Łojkowski, W. 12. Microwaves applied to hydrothermal synthesis of nanoparticles. In *Microwave Chemistry*; De Gruyter: Berlin, Germany, 2017; pp. 205–224. [[CrossRef](#)]
16. Ivill, M.; Pearton, S.J.; Rawal, S.; Leu, L.; Sadik, P.; Das, R.; Hebard, A.F.; Chisholm, M.; Budai, J.D.; Norton, D.P. Structure and magnetism of cobalt-doped ZnO thin films. *New J. Phys.* **2008**, *10*, 065002. [[CrossRef](#)]
17. Wojnarowicz, J.; Chudoba, T.; Gierlotka, S.; Sobczak, K.; Łojkowski, W. Size Control of Cobalt-Doped ZnO Nanoparticles Obtained in Microwave Solvothermal Synthesis. *Crystals* **2018**, *8*, 179. [[CrossRef](#)]
18. Kafle, B.; Acharya, S.; Thapa, S.; Poudel, S. Structural and optical properties of Fe-doped ZnO transparent thin films. *Ceram. Int.* **2016**, *42*, 1133–1139. [[CrossRef](#)]
19. Srinivasulu, T.; Saritha, K.; Reddy, K.R. Synthesis and characterization of Fe-doped ZnO thin films deposited by chemical spray pyrolysis. *Mod. Electron. Mater.* **2017**, *3*, 76–85. [[CrossRef](#)]
20. Wang, J.; Shen, W.; Zhang, X.; Li, J.; Ma, J. Preparation and Characterization of (Al, Fe) Codoped ZnO Films Prepared by Sol-Gel. *Coatings* **2021**, *11*, 946. [[CrossRef](#)]
21. Saadi, H.; Benzarti, Z.; Sanguino, P.; Hadouch, Y.; Mezzane, D.; Khirouni, K.; Abdelmoula, N.; Khemakhem, H. Improving the optical, electrical and dielectric characteristics of ZnO nanoparticles through (Fe + Al) addition for optoelectronic applications. *Appl. Phys. A* **2022**, *128*, 691. [[CrossRef](#)]
22. El Ghoul, J.; Kraini, M.; El Mir, L. Synthesis of Co-doped ZnO nanoparticles by Sol-gel method and its characterization. *J. Mater. Sci. Mater. Electron.* **2015**, *26*, 2555–2562. [[CrossRef](#)]
23. Shi, S.; Yang, Y.; Xu, J.; Li, L.; Zhang, X.; Hu, G.-H.; Dang, Z.-M. Structural, optical and magnetic properties of Co-doped ZnO nanorods prepared by hydrothermal method. *J. Alloys Compd.* **2013**, *576*, 59–65. [[CrossRef](#)]
24. Beltrán, J.J.; Osorio, J.; Barrero, C.A.; Hanna, C.; Punnoose, A. Magnetic properties of Fe doped, Co doped, and Fe+Co co-doped ZnO. *J. Appl. Phys.* **2013**, *113*, 17C308. [[CrossRef](#)]
25. Romeiro, F.C.; Marinho, J.Z.; Lemos, S.C.; de Moura, A.P.; Freire, P.G.; da Silva, L.F.; Longo, E.; Munoz, R.A.; Lima, R.C. Rapid synthesis of Co, Ni co-doped ZnO nanoparticles: Optical and electrochemical properties. *J. Solid State Chem.* **2015**, *230*, 343–349. [[CrossRef](#)]
26. Luo, C.; Ren, X.; Dai, Z.; Zhang, Y.; Qi, X.; Pan, C. Present Perspectives of Advanced Characterization Techniques in TiO₂-Based Photocatalysts. *ACS Appl. Mater. Interfaces* **2017**, *9*, 23265–23286. [[CrossRef](#)] [[PubMed](#)]
27. Kafle, B.P. Introduction to nanomaterials and application of UV-Visible spectroscopy for their characterization. *Chem. Anal. Mater. Charact. Spectrophotom.* **2019**, 147–198. [[CrossRef](#)]

28. Uklein, A.; Multian, V.; Kuz'Micheva, G.; Linnik, R.; Lisnyak, V.; Popov, A.; Gayvoronsky, V.Y. Nonlinear optical response of bulk ZnO crystals with different content of intrinsic defects. *Opt. Mater.* **2018**, *84*, 738–747. [[CrossRef](#)]
29. Paskaleva, A.; Blagoev, B.S.; Terziyska, P.T.; Mehandzhiev, V.; Tzvetkov, P.; Kovacheva, D.; Avramova, I.; Spassov, D.; Ivanova, T.; Gesheva, K. Structural, morphological and optical properties of atomic layer deposited transition metal (Co, Ni or Fe)-doped ZnO layers. *J. Mater. Sci. Mater. Electron.* **2021**, *32*, 7162–7175. [[CrossRef](#)]
30. Pekar, G.; Singaevsky, A.; Kolomys, O.; Strelchuk, V.; Lytvyn, P.; Osipyonok, M.; Vasin, I.; Skoryk, M. Magnetic and optical properties of printed ZnO:Co polycrystalline layers. *Mater. Sci. Semicond. Process.* **2021**, *135*, 106054. [[CrossRef](#)]
31. Özgür, Ü.; Alivov, Y.I.; Liu, C.; Teke, A.; Reshchikov, M.A.; Doğan, S.; Avrutin, V.; Cho, S.-J.; Morkoç, H. A comprehensive review of ZnO materials and devices. *J. Appl. Phys.* **2005**, *98*, 041301. [[CrossRef](#)]
32. Singh, R.P.P.; Hudiara, I.S.; Panday, S.; Rana, S.B. Effect of Ni Doping on Structural, Optical, and Magnetic Properties of Fe-Doped ZnO Nanoparticles. *J. Supercond. Nov. Magn.* **2015**, *28*, 3685–3691. [[CrossRef](#)]
33. Tariq, M.; Li, Y.; Li, W.-X.; Yu, Z.-R.; Li, J.-M.; Hu, Y.-M.; Zhu, M.-Y.; Jin, H.-M.; Liu, Y.; Li, Y.-B.; et al. Structural, ferromagnetic, and optical properties of Fe and Al co-doped ZnO diluted magnetic semiconductor nanoparticles synthesized under high magnetic field. *Adv. Manuf.* **2019**, *7*, 248–255. [[CrossRef](#)]
34. Straumal, B.; Protasova, S.G.; Mazilkin, A.A.; Tietze, T.; Goering, E.; Schütz, G.; Straumal, P.; Baretzky, B. Ferromagnetic behaviour of Fe-doped ZnO nanograined films. *Beilstein J. Nanotechnol.* **2013**, *4*, 361–369. [[CrossRef](#)] [[PubMed](#)]
35. Subramanian, A.M.; Thakur, P.K.; Tanemura, M.; Hihara, T.; Ganesan, V.; Soga, T.; Chae, K.H.; Jayavel, R.; Jimbo, T. Intrinsic ferromagnetism and magnetic anisotropy in Gd-doped ZnO thin films synthesized by pulsed spray pyrolysis method. *J. Appl. Phys.* **2010**, *108*, 053904. [[CrossRef](#)]